Energy & Environmental Science

Conditions for Stable Operation of Solid Oxide Electrolysis Cells: Oxygen Electrode Effects

Journal:	*Energy & Environmental Science*
Manuscript ID	EE-ART-05-2019-001664.R1
Article Type:	Paper
Date Submitted by the Author:	09-Jul-2019
Complete List of Authors:	PARK, BEOM-KYEONG; Northwestern University, Materials Scinence and Engineering Zhang, Qian; Northwestern University, Materials Scinence and Engineering Voorhees, Peter; Northwestern University, Materials Science and Engineering Barnett, Scott; Northwestern University, Materials Science and Engineering

ARTICLE

Conditions for Stable Operation of Solid Oxide Electrolysis Cells: Oxygen Electrode Effects

Received 00th January 20xx,
Accepted 00th January 20xx

DOI: 10.1039/x0xx00000x

Beom-kyeong Park,[a] Qian Zhang,[a] Peter W. Voorhees [a] and Scott A. Barnett *[a]

Solid oxide electrolysis cells (SOECs) convert renewable electricity to fuels with efficiency substantially higher than other electrolysis technologies. However, questions remain regarding degradation mechanisms that limit SOEC long-term stability. One of the key degradation mechanisms is oxygen electrode delamination; although prior studies have improved the understanding of this mechanism, it is still difficult to predict how degradation depends on SOEC materials and operating conditions, *i.e.*, temperature, voltage, and current density. Here we present a study aimed at developing a quantitative understanding of oxygen electrode delamination. Experimentally, a life test study of symmetric and full cells with yttria-stabilized zirconia (YSZ) electrolytes and Gd-doped Ceria (GDC) barrier layers was done with three different perovskite oxygen electrode materials. Fracture was observed at the perovskite-GDC interface above a critical current density and below a critical operating temperature. A theory is presented that combines a calculation of the effective oxygen pressure across the electrolyte with an estimation of the pressure required for fracture. Fracture is correctly predicted for a critical oxygen partial pressure of ~7200 atm and an associated electrode overpotential of ~0.2 V, occurring at the electrode/GDC interface because of the relatively low perovskite fracture toughness. Damage at the GDC/YSZ interface was also observed in some cases and explained by a peak in the oxygen pressure at this interface.

Broader context

The International Renewable Energy Agency has determined that half of the CO_2 emissions reductions needed to limiting global warming to 2 ^oC can be achieved by increasing renewables such as wind and solar to 36 % of energy production by 2030.[1] However, these renewables provide an intermittent and in some cases unpredictable supply; when they exceed ~20 % of total electricity generation, energy storage is required to match supply with demand while avoiding curtailment.[2] The SOEC technology addressed in this report is a promising contender for large-scale grid electricity storage[3] and for conversion of excess renewable electricity to useful fuels for transportation and other applications.[4] Given that good long-term stability is a key requirement for viability of this technology, the fundamental understanding of oxygen-electrode degradation phenomena developed in the present study is expected to play an important role in its further development.

1. Introduction

High capacity grid-scale electricity storage is increasingly required as intermittent renewable sources such as wind and solar are increased above 20 % of grid electricity supply.[2] Although many energy storage methods have been proposed and explored,[5,6] only pumped hydroelectric storage has seen significant application; however, its geographic availability is limited. Other technologies require significant further development to meet the requisite cost, efficiency, and energy capacity requirements for grid-scale storage on the time frame required – days to months. One technology that has potential, but that has only recently received widespread attention, is the solid oxide cell (SOC). One key advantage of SOCs is that gaseous fuels are produced during electrolysis operation, such that storage capacity can be increased by increasing storage tank size.[7] This is similar to flow batteries, but with the additional advantage that the storage media (*e.g.*, H_2, CH_4) are derived from very low cost feedstocks (H_2O and CO_2) compared to liquid anolyte and catholyte solutions. SOCs can be operated reversibly – part time storing energy in electrolysis mode and part time generating electricity in fuel cell mode.[3,8,9] Alternatively, SOCs solely in electrolysis mode can be utilized to convert excess renewable electricity to produce fuels, *e.g.*, H_2, CH_4, or Fischer-Tropsch liquids, that can be stored for later use in applications such as transportation.[4] Because of their high operating temperatures, SOCs can have relatively low area-specific resistance, allowing high conversion efficiencies of ~90 % for electricity to fuel[4,10] and > 70 % for round-trip electricity storage.[3,11] It has also been shown that combining SOCs with biomass gasification can greatly improve productivity, *e.g.*, doubling the methanol output from wood biomass.[12]

Although the above applications are similar to solid oxide fuel cells, a technology currently undergoing commercialization, there are significant new challenges. In particular, electrolysis and reversible operation of SOCs lead to new degradation mechanisms not observed in fuel cell operation. Many of these

[a] *Department of Materials Science and Engineering, Northwestern University, Evanston, Illinois 60208, USA, E-mail: s-barnett@northwestern.edu*

† Electronic Supplementary Information (ESI) available: See DOI: 10.1039/x0xx00000x

arise because of the higher potential across the SOC in electrolysis mode compared to fuel cell mode, which drives extremes of oxygen partial pressure within the SOC.[13–16] One degradation mechanism that has been widely reported is the delamination of the oxygen electrode, typically $(La_{0.8}Sr_{0.2})MnO_3$ (LSM)–8 mol.% Y_2O_3-doped ZrO_2 (YSZ), from the electrolyte,[16–27] often *via* the formation of oxygen bubbles in the electrode/electrolyte region.[16] It was also shown that increasing the current density accelerated the degradation,[28] but that periodically reversing the current (from electrolysis into fuel cell mode) reduced the degradation.[28,29] These experimental findings have been explained by the high oxygen pressure induced within the electrolyte by the applied oxygen electrode overpotential,[13,15,16] although alternate mechanisms have been proposed such as the volume expansion or contraction of the electrode due to changes in oxygen stoichiometry.[26] Virkar proposed that delamination could be explained by the oxygen pressure exceeding the fracture strength of the electrolyte.[15] On the other hand, SOCs with the LSM–YSZ electrode replaced by the mixed ionically and electronically conducting (MIEC) electrode $(La_{0.6}Sr_{0.4})(Co_{0.2}Fe_{0.8})O_3$ (LSCF) showed fairly stable electrolysis operation without evidence of interfacial fracture,[30] although gradual degradation due to Sr segregation is sometimes observed. The reasons for these differences are not fully understood, although it is reasonable to expect that LSCF avoids fracture due to lower overpotentials associated with its lower polarization resistance R_p compared to LSM–YSZ. Nonetheless, the current understanding is incomplete, such that delamination effects cannot be accurately predicted for any specific type of LSM–YSZ or LSCF electrode, not to mention other MIEC electrodes. In particular, degradation is known to increase with increasing current density, apparently due to the associated overpotential increase, but the effects of other parameters such as temperature and electrode composition are generally not known. In addition to delamination, damage within the electrolyte is observed during electrolysis in some cases,[16 17,20,24,27,30] but this effect has not been explained.

Here we present a systematic study of degradation related to the oxygen electrode in SOCs operated in electrolysis mode. Three different oxygen electrode materials were studied: LSCF along with $Sr(Ti_{0.3}Fe_{0.7})O_3$ (STF) and $Sr(Ti_{0.3}Fe_{0.63}Co_{0.07})O_3$ (STFC). The latter two compositions are MIEC materials that provide different polarization resistances R_p than LSCF, providing insights into how the R_p value impacts degradation. In addition, they are more stable during life tests than LSCF,[31] making the data interpretation more straightforward. Whereas most prior studies have focused on the effect of current density, here the effect of operating temperature is also fully explored. Many of the tests were done with oxygen-electrode symmetric cells in order to simplify data interpretation, to avoid extraneous degradation effects from the fuel electrode in full cells, and to help enable measurements of the electrode overpotential. The life test electrochemical data is augmented by post-test microstructural/chemical evaluation. The experimental work is complemented by a theory where the oxygen potentials across the electrolyte were numerically derived and the resulting effective oxygen partial pressure values compared with the fracture condition for the relevant materials – the YSZ electrolyte, the GDC barrier layer, and the perovskite oxide electrode. The theory predicts that the fracture occurs primarily at the electrode/GDC interface, and correctly predicts the critical values of oxygen pressure and electrode overpotential that initiate failure. The combined results are used to provide SOC stability maps for the different electrodes in terms of current density and operating temperature, and also used to explain prior literature data for LSM–YSZ and LSCF.

2. Results

Life tests on full cells are also presented in section 2.1. Systematic studies on symmetric cell stability include the effects of operating conditions, *i.e.,* temperature (T) and current density (j) (section 2.2) and electrode material (section 2.3). Measurements of symmetric cells with potential probes to determine electrode overpotentials is described in section 2.4.

2.1 Full Cell Life Tests

Effects including oxygen electrode delamination and oxygen bubble formation have been reported previously for SOECs with LSM–YSZ oxygen electrodes. However, such effects are not normally seen in cells with MIEC electrodes such as LSCF.[30,32–34] Here we show results for Ni–YSZ fuel-electrode-supported cells tested under electrolysis operating conditions, demonstrating that these effect can occur under some conditions. One cell, with an STFC oxygen electrode, was tested at 1 A cm^{-2} at 800 °C, and one with an STF oxygen electrode was tested at 0.8 A cm^{-2} at 600 °C. Fig. 1(a) exhibits the evolution of cell voltage for both cells. The STFC cell voltage increased gradually over the first few hundred hours, and appeared to be stabilizing by the end of the 400 h test. The STF-electrode cell showed instability as well as fluctuation in voltage and failed within ~17 h. Fig. 1(b) shows post-test SEM images – the 800 °C-tested cell showed a structure similar to that observed for an untested cell, consistent with the symmetric cell results that showed stable operation for higher temperatures. The 600 °C-tested cell showed extensive fracturing at the electrode/GDC interface.

One feature seen in Fig. 1(b) is that the electrolyte surface near the GDC/YSZ interface revealed a grain boundary structure, different than the planar surfaces seen in the other SEM images. Note that the imaged surfaces were produced by fracture, and the observed intergranular fracture suggests that grain boundaries were weak in this case. The magnified view of this regions, shown in the inset in Fig. 1(b), shows that voids were present along the grain boundaries, explaining the intergranular fracture. Grain boundary void formation near the electrode/electrolyte interface during high-current electrolysis operation has been reported previously.[16]

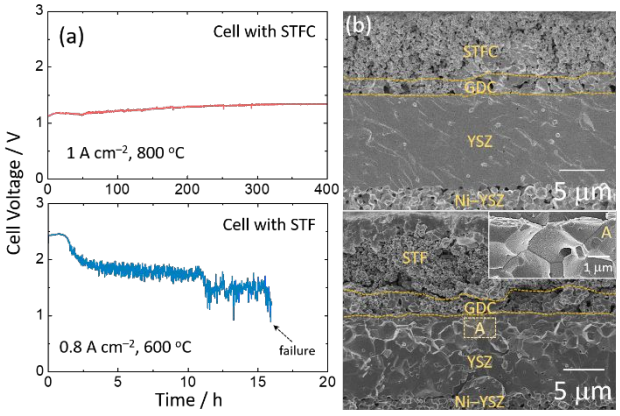

Fig. 1 (a) Cell voltage *vs.* time for NiO–YSZ supported SOECs with STFC and STF tested with j = 1 A cm^{-2} at 800 °C and with j = 0.8 A cm^{-2} at 600 °C, respectively. (b) Cross-sectional SEM images for Ni–YSZ supported SOECs with STFC and STF after the life tests. Note that the fracture in (b) is at the interface between the STF electrode and the porous GDC layer.

2.2 Symmetric Cells – Effect of Temperature and Current Density

Fig. 2 shows representative examples of EIS spectra data taken during life tests of identically-prepared STF-electrode symmetric cells tested in air with constant current density j = 0.8 A cm^{-2} at temperature T = 600 (a) or 650 °C (b), and j = 1.6 A cm^{-2} at T = 650 °C (c). The impedance spectra were measured periodically during brief interruptions of the cell current. The high frequency intercept with the real axis, which was shown to correspond with good accuracy to the electrolyte ohmic resistance (R_Ω), and the difference between the high and low frequency intercepts, which was shown to correspond to the electrode polarization resistance (R_p), are plotted versus time in Fig. 3. The R_Ω and R_p values remain approximately constant throughout the test for 650 °C and 0.8 A cm^{-2}. Longer tests carried out to ~1000 h showed that cells remain stable (Fig. S1). However, the other tests showed relatively unstable R_p values before failing within 50 – 200 h of testing.

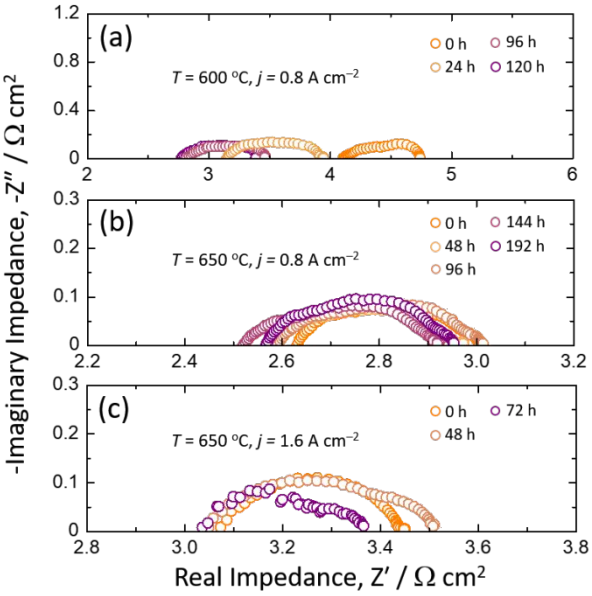

Fig. 2 Nyquist plots obtained from life tests of STF-electrode symmetric cells tested in air with constant current density j = 0.8 A cm^{-2} at temperature T = 600 (a) or 650 °C (b), and j = 1.6 A cm^{-2} at T = 650 °C (c).

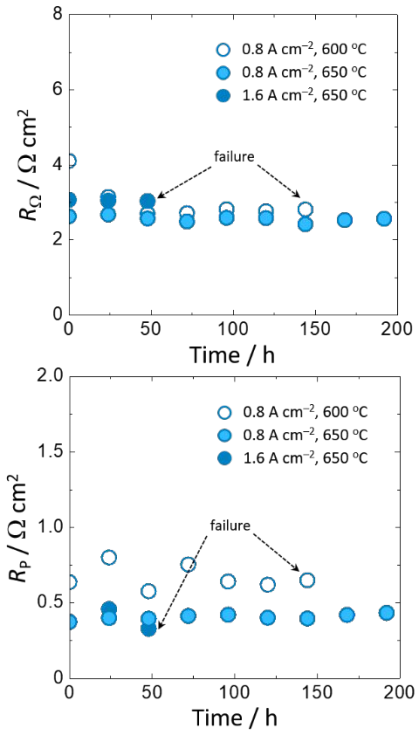

Fig. 3 Evolution of ohmic resistance (R_Ω) and polarization resistance (R_p) with time for STF-electrode symmetric cells tested in air with constant current density j = 0.8 A cm^{-2} at temperature T = 600 or 650 °C, and j = 1.6 A cm^{-2} at T = 650 °C.

Figs. 4(a)–(c) show fracture cross-sectional SEM images of the electrolysis-side electrodes after the cell life tests. For the cell tested at T = 650 °C and j = 0.8 A cm^{-2} (b), there was no sign of fracture and/or delamination at the electrolysis side – the structures appear

identical to those of the electrodes prior to testing, shown in Fig. S2. Note that visible pores across the electrolyte were generated though our cell fabrication process, not by the build-up of high oxygen pressure under the current application. However, decreasing T to 600 °C (a) or increasing j to 1.6 A cm^{-2} (c) resulted in obvious fracture at the electrode, presumably explaining the cell failures illustrated in Fig. 3. In Fig. 4(a), there also appears to be a fracture near the GDC/YSZ interface. On the other hand, the microstructures of the fuel-cell sides of these cells, shown in Fig. S3 in the supplement, appeared unchanged from the pre-test case.

Note that the condition shown in Fig. 4(a) is the same as that for one of the full cell tests shown in Fig. 1, and both show similar delamination at the electrode/GDC interface. Similarly, for the symmetric cell operated at the same condition as the other full cell shown in Fig. 1, at 800 °C (see supplemental Fig. S4), both cells showed stable operation with no evidence of fracture. These results provide an initial indication that the symmetric cell results are in agreement with the full cell data. Note that Fig. 4(a) shows an apparent fracture near the GDC/YSZ interface, the same region where damage was present in the corresponding full cell in Fig. 1(b).

SEM–EDS line scans were done in order to determine the location of the fractures. The example shown here is for T = 600 °C and j = 0.8 A cm^{-2}. Fig. 4(a) shows the position of the line scan on the image and Fig. 5 shows the resulting compositional profile. It is clear that the fracture occurred at the STF/GDC interface; note that the fracture appears to be within the electrode because GDC barrier layer has a similar porous structure to the STF electrode. Note that prior reports of LSM–YSZ delamination during the SOEC operation also showed delamination at the interface.[16,18,23,26]

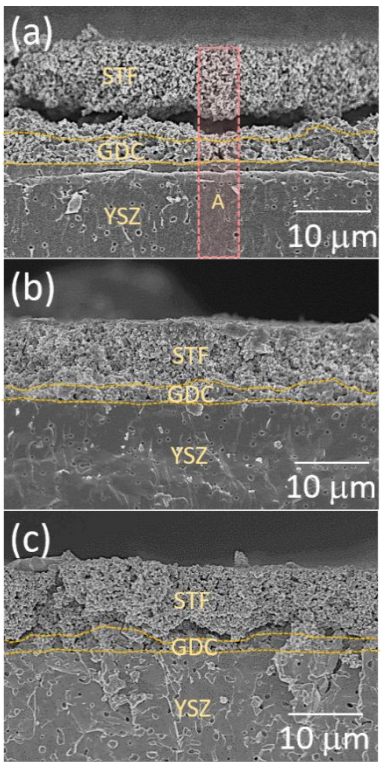

Fig. 4 Cross-sectional SEM images (fractured surface) taken from STF-electrode symmetric cells tested with j = 0.8 A cm^{-2} at T = 600 (a) or 650 °C (b), and j = 1.6 A cm^{-2} at T = 650 °C (c) after life tests.

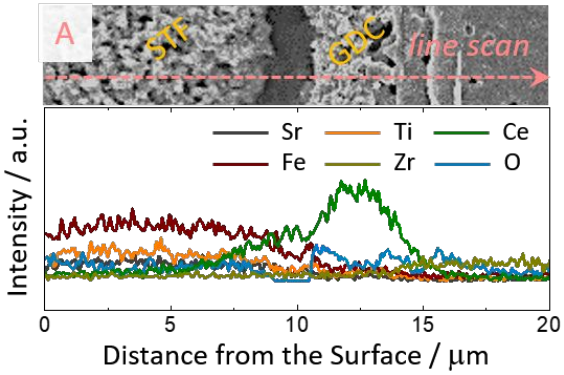

Fig. 5 Concentration profiles of Sr, Ti, Ce, Fe, Zr, and O across the electrode and electrolyte, in the area labelled "A" in Fig. 4(a). This shows that the fracture in Figure 4(a) is at the interface between the STF electrode and the porous GDC layer, not within the electrode.

2.3 Symmetric Cells – Effect of Electrode Material

The results presented above are compared with those from cells with two other electrode materials: LSCF and STFC. STFC, or Co-doped STF, has been shown to have a substantially lower R_p than STF, thus providing an indication of how R_p affects stability. LSCF, on the other hand, provides a higher R_p than STF or STFC, and is also a useful comparison because it is a widely used electrode material. However, LSCF provides some complication because its R_p value tends to vary with time due to Sr segregation.[31,35–38]

Symmetric cells with STFCs were tested at j = 0.8 and 1.6 A cm^{-2} at 600 °C, and the resultant EIS data and post-test SEM images are shown in Figs. 6(a) and 6(b), respectively. The R_p of ~0.5 Ω cm^2 for the STFC cell was lower than for STF (~0.7 Ω cm^2). The cell was stable and showed no fracture for 0.8 A cm^{-2} at 600 °C, at conditions where the STF cell failed via fracture. That is, a lower R_p electrode can help avoid failure due to fracture. However, increasing j to 1.6 A cm^{-2} resulted in failure *via* fracture of the STFC cell after < 80 h.

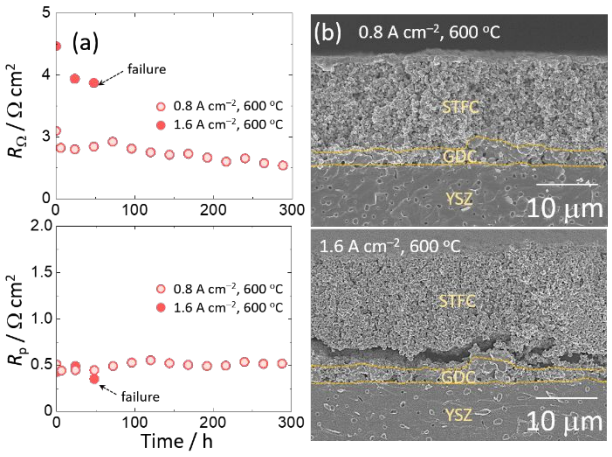

Fig. 6 (a) Evolution of ohmic resistance (R_Ω) and polarization resistance (R_p) with time for STFC-electrode symmetric cells tested with different current densities of 0.8 and 1.6 A cm^{-2} at

600 °C. (b) Cross-sectional SEM images taken from the STFC-electrode symmetric cells after the life tests. Note that the fracture in (b) is at the interface between the STFC electrode and the porous GDC layer.

Fig. 7(a) and 7(b) exhibit measured R_Ω and R_p values *vs*. time and post-test SEM images, respectively, for LSCF-electrode cells for cells life tested with j = 0.8 A cm^{-2} at 600 and 650 °C. The LSCF cells both failed during the life tests, showing fractures at the electrode/electrolyte interfaces after the life tests. The failure at 650 °C occurred later, after ~170 h, compared to ~120 h for 600 °C. This might be explained by the continuous increase in R_p for the higher temperature test, which can be explained by Sr segregation kinetics being faster at the higher temperature.[35,38] Thus, the cell failure may have been delayed until R_p became large enough to cause fracture. Note that for 0.4 A cm^{-2} and 600 °C, the LSCF cells were stable (Fig. S5).

Fig. 8 summarizes the various life tests performed in this study, showing the cases where failure occurred and where the cells were stable. Comparison of the results for STF, LSCF, and STFC electrodes indicates that electrode delamination is dependent on the electrode type, and occurs more readily at higher current density and lower temperature.

Comparison with the STF-electrode full cell test done under the same conditions (j = 0.8 A cm^{-2} and T = 600 °C) (Fig. 2(a)) showed similar failure. The symmetric cell results are thus consistent with the full cell results.

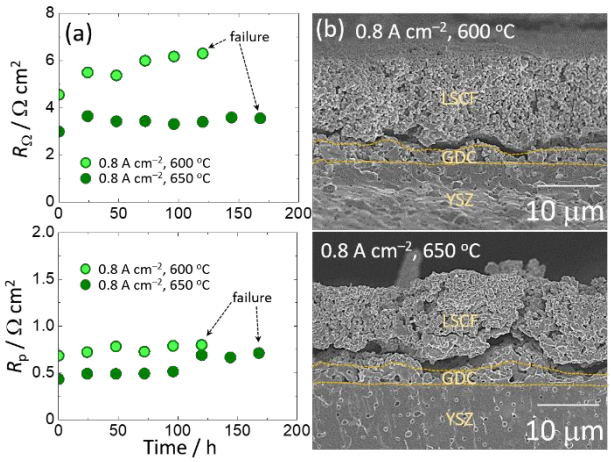

Fig. 7 (a) Evolution of ohmic resistance (R_Ω) and polarization resistance (R_p) with time for LSCF-electrode symmetric cells tested with a constant current densities of 0.8 A cm^{-2} at 600 and 650 °C. (b) Cross-sectional SEM micrographs taken from the LSCF-electrode symmetric cells after the life tests. Note that the fracture in (b) is at the interface between the LSCF electrode and the porous GDC layer.

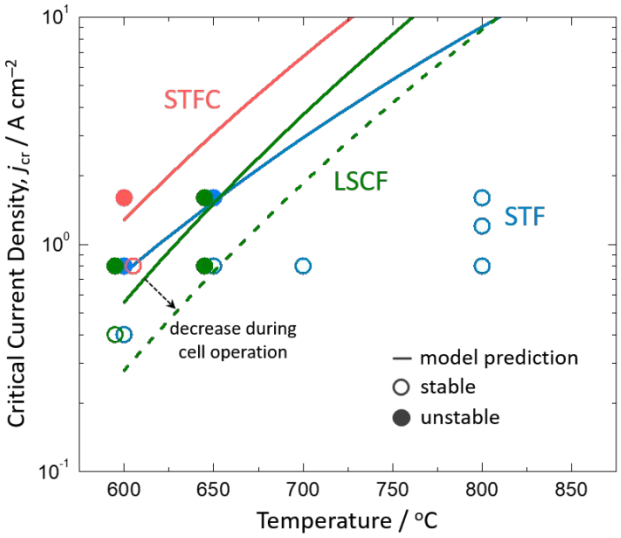

Fig. 8 A critical current density (j_{cr}) *vs*. temperature diagram for the electrode/electrolyte interface fracture.

2.4 Estimation of Electrode Overpotential

In order to evaluate the role of overpotential in the observed cell failure, the following two measurements were carried out and analyzed. An Ag-ink potential probe was painted around the edge of the symmetric cell electrolyte pellets; this was in addition to the two identical working electrodes that were applied to opposite sides of the pellet.

First, the potential probe was used to determine if the current-voltage relation for the electrode is symmetrical with current direction, or is different in fuel-cell and electrolysis modes. DC current was run through the cell and the voltage of each electrode relative to the Ag electrode was measured. It was found that the voltage was always slightly higher on one side of the cell regardless of the current direction. This indicates that there was some asymmetry in the cell, most likely in the potential probe placement. The cell asymmetry effect was eliminated by averaging the electrolysis-side voltages measured for opposing current directions. Comparison with similarly averaged fuel-cell-side voltages yielded agreement of the voltages to within 0.1 % (see supplemental Table S1). That is, the current-voltage curve was symmetric. Since the voltage drop across electrolyte is certainly expected to be symmetrical with current direction, this indicates that the electrode overpotentials in the two current directions must also be essentially symmetric. Thus, the electrolysis electrode overpotential can be taken as half of the total electrode overpotential.

Second, impedance measurements were carried out using the two working electrodes over a range of current densities j (see Fig. S6). The spectra were fit using a previously-reported model for the STF electrodes[31] and the polarization resistance R_p values were obtained. Fig. 9 shows the resulting R_p values for one electrode (half the total measured polarization resistance) plotted versus j at various measurement temperatures. Since $\boldsymbol{R_p = \frac{\partial \eta}{\partial j}}$, the overpotential can be obtained by integrating

$$\eta(j) = \int_0^j \eta = \int_0^j R_p dj' \qquad (1)$$

Numerical integration of the data in Fig. 9 was done following eqn (1), and the results are shown in Fig. 10. The Butler-Volmer equation was used for comparison with these results – it should be valid if the main rate-limiting step of the electrode process is charge-transfer. A simple symmetric form of the equation was utilized in which the symmetry coefficient α = 0.5, yielding:

$$\eta = \frac{2RT}{zF}\sinh^{-1}\left(\frac{j}{2j_0}\right) \qquad (2)$$

where R is the gas constant, F is Faraday's constant, z = 2 is the charge in the relevant reaction, and the exchange current density j_0 is obtained using the measured zero-current polarization resistance R_p (j=0):

$$j_0 = \frac{RT}{zFR_p(j=0)} \qquad (3)$$

Fig. 10 shows the variation of η with j obtained from eqn (2) and (3). Since the zero-current value of R_p is used in obtaining the calculated curves, they must agree with the low current η values obtained by integrating the R_p data. However, at higher j values, there is some deviation, indicating a deviation from the idealized Butler-Volmer form. Nonetheless, it can be seen that a measured R_p (j=0) value can be used with eqn (2) and (3) to provide estimated η values.

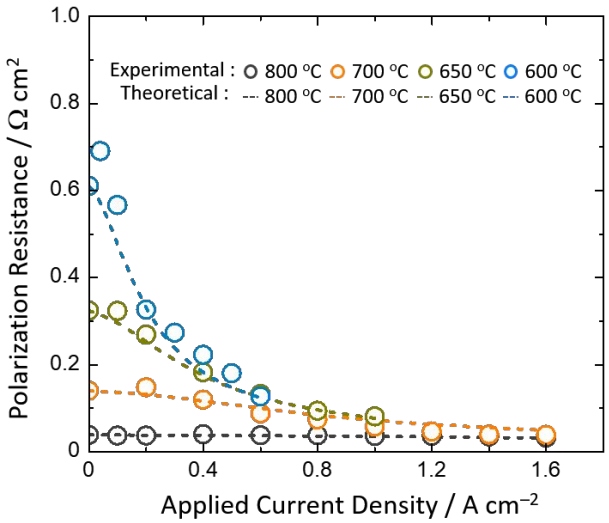

Fig. 9 Comparison of experimentally measured and theoretically estimated polarization resistances using different current densities at 600, 650, 700, and 800 °C. The measured values are compared with predicted values – the latter obtained by taking the derivative of eqn (2), giving $R_p(j) = \frac{\partial \eta}{\partial j} = \frac{RT}{zFj_0\sqrt{1+\left(\frac{j}{2j_0}\right)^2}}$

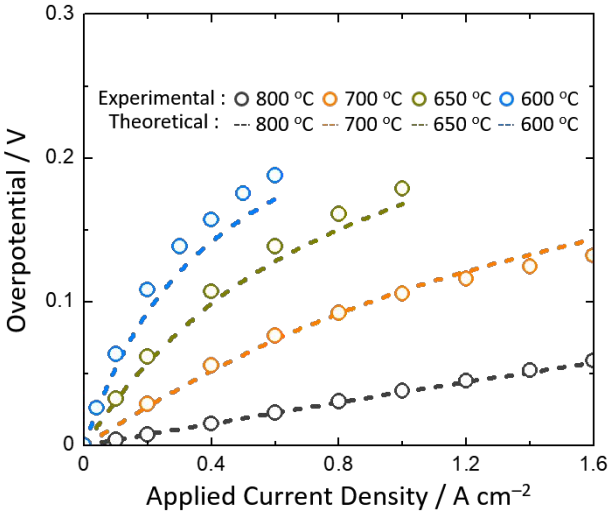

Fig. 10 Comparison of experimentally measured and theoretically estimated electrode overpotentials using different current densities at 600, 650, 700, and 800 °C.

3. Discussion

Using the above results, we can test the idea that cell failure is determined by the electrode overpotential. Based on eqn (2) and (3), results for R_p versus time (*e.g.*, as shown in Figs. 3, 6, and 7) can be re-cast as η versus time, as shown in Fig. 11 for STF (a), STFC (b), and LSCF (c). In life tests where η stayed below ~200 mV, the cell performance remained stable and SEM images showed no structural degradation. In tests with $\eta \geq 200$ mV, the cells failed. The life test of LSCF performed at 0.8 A cm^{-2} and 650 °C provides a case where there was a continuous increase in R_p and η due to Sr segregation; the cell was stable in the first 100 h while η remained below 200 mV, but the cell failed ~50 h after η exceeded 200 mV, at ~120 h of testing. In summary, fracture occurs at the electrode/electrolyte interface when the η value exceeds ~200 mV, irrespective of the electrode material.

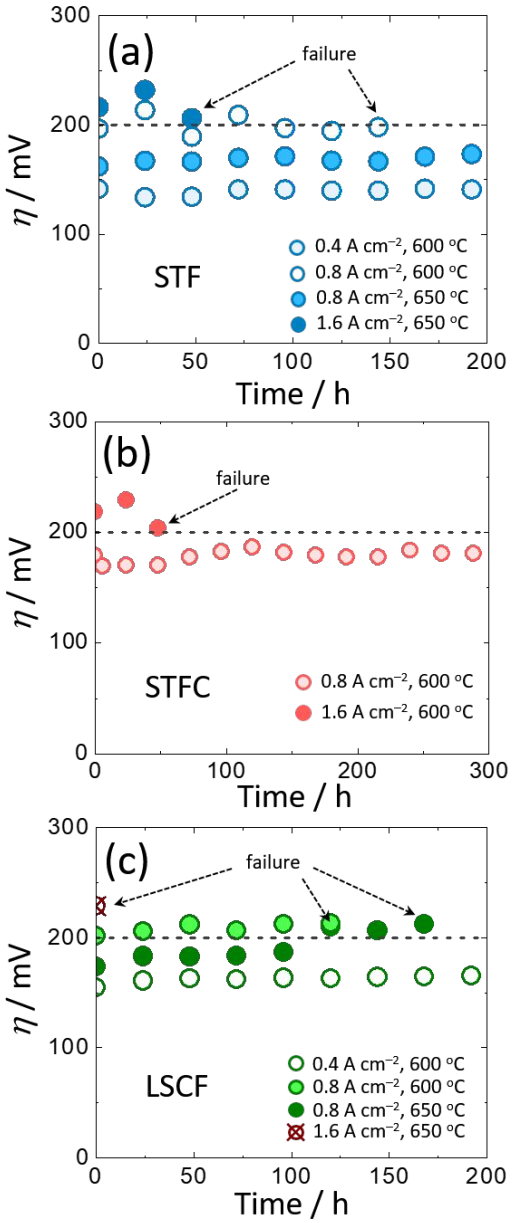

Fig. 11 The electrode overpotential (η) values of (a) STF, (b) STFC, and (c) LSCF for various symmetric cell testing conditions. The dotted line indicates a critical electrode overpotential of 200 mV.

Additional questions remaining regarding the present results include:

1) Are the full cell and symmetric cell expected to show the same degradation behaviors?

2) Can the observed cell degradation – fracture at the perovskite/GDC interface and grain boundary void formation in the region near the YSZ/GDC interface – be explained?

3) Can the magnitude of the overpotential required for fracture, ~200 mV, be understood based on materials fracture behavior?

To help answer these questions, a mathematical electrolyte model (presented in the supplemental material) was employed that is similar to that reported previously.[39–42] Fig. 12 shows the calculated P_{O_2} versus position across the electrolyte, for symmetric and full cells with STF oxygen electrode at 800 °C and j = 0.8 A cm^{-2}. The full cell shows a very low P_{O_2} on the fuel side, substantially lower than the value associated with the fuel gas composition – low enough values can lead to fuel electrode degradation.[43] Even though the symmetric cell thickness is > 20 times that of the full cell, and air is maintained on both sides, the P_{O_2}versus position near the oxygen electrode is nearly identical. Both show that a maximum P_{O_2} is reached at the GDC/YSZ interface, which results from the higher ratio of conductivity of holes to conductivity of ions of GDC compared to YSZ. Thus, symmetric cell results should provide a good surrogate for full cells for determining oxygen electrode degradation. This helps explain the good agreement between the full cell and symmetric cell results.

Fig. 13 shows the P_{O_2} distribution for a range of different current density and temperature, for the three different electrode materials. Also shown in Fig. 13 are the critical oxygen pressure (P_{cr}) values for fracture,[44] given by:

$$P_{Cr} = \frac{1}{2}\sqrt{\frac{\pi}{(1-\upsilon^2)c}}K_{Ic} \quad (4)$$

where K_{Ic} is the fracture toughness, the initial defect size c is taken to be 1 μm corresponding to the size of pores in the electrolyte, the Poisson ratio v is 0.3 for YSZ,[45] 0.33 for GDC,[46] and 0.24 for perovskite.[47] The fracture toughness values and resulting critical oxygen pressures for YSZ, GDC, and perovskite oxides are summarized in Table 1 and are also shown in Fig. 13. Note that exact fracture toughness values for the specific electrode materials are not known, so we have used a generic value for perovskite materials.[47] Fig. 13 shows that no fracture is expected in YSZ except for the most extreme conditions tested here – *e.g.*, j = 1.6 A cm^{-2}, T = 600 °C – in good agreement with the experimental observations. On the other hand, the P_{O_2} values at the electrode/GDC interface are close to or higher than the P_{cr} of perovskite oxide at the conditions where interfacial fracture occurs.

Note that with the fracture occurring at the electrolyte/electrode interface, where the P_{O_2} relative to the ambient gas-phase pressure $P_{O_2,amb}$ is set by the overpotential boundary condition,

$$\frac{P_{O_2}}{P_{O_2,amb}} = exp\left(\frac{4F\eta}{RT}\right) \quad (5)$$

the fracture condition is fully specified by the overpotential. This explains why the overpotential is a good predictor of cell failure in Fig. 11. By combining eqn (4) and (5) with $P_{O_2} = P_{Cr}$, we obtain an expression that directly relates fracture toughness to critical overpotential:

$$\eta_{Cr} = \frac{RT}{4F} ln\left(\frac{\pi^{1/2}K_{Ic}}{2(1-\upsilon^2)^{1/2}c^{1/2}P_{O_2,amb}}\right) \quad (6)$$

where the ambient oxygen pressure $P_{O_2,amb}$ is 21.3kPa. This expression is as given by Virkar.[15] The predicted values are given in Table 1. The value for the perovskite, 196 mV, is in good agreement with the overpotential experimentally observed to cause fracture of ~200 mV (Fig. 10). If we further assume that $\eta(j)$ is given by the simplified Butler-Volmer dependence (eqn

(2) and (3)) and that R_p usually follows an Arrhenius dependence (given in Table S2),

$$R_{P,O}(j=0) = R^0_{P,0} exp\left(\frac{E_P}{RT}\right) \quad (7)$$

Combining eqn (2), (3), (6), and (7) yields an expression for the critical current density for fracture,

$$j_{Cr} \approx \frac{RT}{FR^0_P \exp\left(\frac{E_P}{RT}\right)} \sinh\left[\frac{1}{4} ln\left(\frac{\pi^{\frac{1}{2}} K_{Ic}}{2(1-\upsilon^2)^{\frac{1}{2}} c^{\frac{1}{2}} P_{O_2,amb}}\right)\right] \quad (8)$$

The approximate sign is used because the simplified Butler-Volmer equation is approximate. The predicted j_{cr} *vs.* temperature is shown in Fig. 8, compared with the experimental results for fracture or non-fracture for STF, STFC, and LSCF electrodes previously shown. Since the R_p value for STF and STFC electrodes remains stable during the life tests, we can construct a single j_{cr} line to determine the electrode/electrolyte interface stability. STFC has a higher j_{cr} value than STF owing to its lower R_p. The model predictions agree well with the experimental findings. For LSCF, the initial j_{cr} values (solid line in Fig. 8) shift to lower values (dashed line) during cell operation due to a segregation-induced increase in R_p. Thus, the model correctly predicts that the fracture occurs at the GDC/perovskite interface, and also correctly predicts the magnitude of the critical overpotential (or j value) above which fracture occurs. It is very difficult to directly measure the overpotential in full anode-supported cells, but it can be assumed that identically-prepared electrodes in symmetric and full cells have the same polarization resistance, and hence the same overpotential at a given current density. Thus, it is not surprising that the full-cell electrodes (Fig. 1) are observed to fracture under the same conditions as the symmetric cell electrodes.

Figs. 12 and 13 also show that the peak P_{O_2} values at the GDC/YSZ interface can reach values high enough for GDC fracture. Such a fracture was observed in the STF-electrode symmetric cell test at 0.8 A cm^{-2} and 600 °C (Fig. 4(a)). However, in the full cell test under this same condition, grain boundary voids appear in the region near the GDC/YSZ interface. It is not clear why the degradation mechanism is different in this case; however, it seems likely that a pressure high enough to cause fracture could also induce void formation.[16]

Table 1. Critical oxygen pressure (P_{cr}), critical oxygen electrode overpotential (η_{cr}), and fracture toughness values for YSZ, GDC, and perovskite oxide (ignoring any influence of temperature on the fracture toughness).[44,46]

Material	P_{cr} (atm)	η_{cr} (mV) at 600 °C	K_{1c} (MPa m$^{1/2}$)
YSZ	27500	222	3
GDC	13900	209	1.5
Perovskite	7200	196	0.8

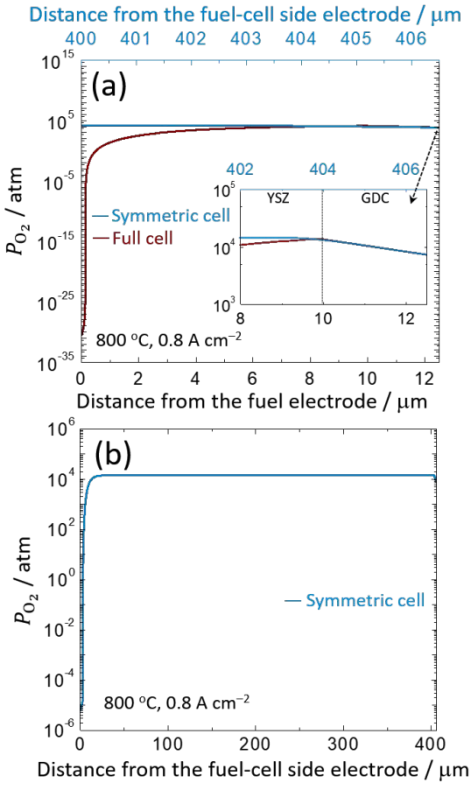

Fig. 12 (a) Comparison of the calculated oxygen partial pressure P_{O_2} versus position in the electrolytes of full and symmetric cells at 600 °C with j = 0.8 A cm^{-2} with air at the STF oxygen electrodes. The full cell had 50 % fuel at the Ni–YSZ fuel electrode. (b) shows the P_{O_2} versus position across the entire thickness of the electrolyte.

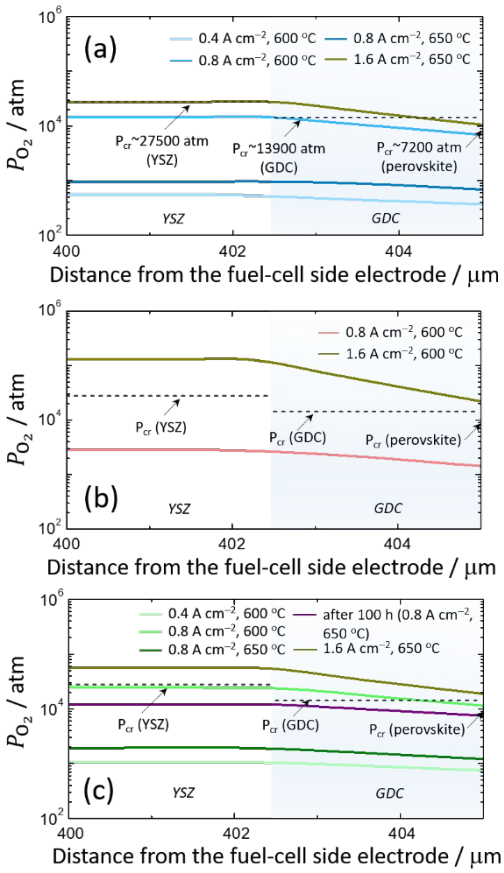

Fig. 13 Distribution of the oxygen partial pressure across the electrolyte thickness for the symmetric cells with (a) STF, (b) LSCF, and (c) STFC electrodes under various life testing conditions. The plots show only the critical region near YSZ/GDC interface and the GDC/electrode interface – the remainder of the electrolyte shows a constant P_{O_2} value over most of its thickness with an abrupt decrease near the fuel electrode, as shown in Fig. 12(b).

The present theory can also be compared with prior reports of SOC fracture during electrolysis – the available data is for LSM–YSZ and LSCF electrodes.[16,17,19–27,30,32–34,48,49] Fig. 14 shows the predicted j_{cr} values versus temperature using eqn 8 compared with the experimental conditions for fracture or non-fracture. For LSM–YSZ, fracture is mostly observed at $j \gtrsim 1$ A cm^{-2}, with stable operation at lower j. The results are mostly in agreement with the calculated j_{cr} curve, which is at relatively low j values because of the relatively high R_p of LSM–YSZ. For LSCF, fracture has not been observed because maximum j values employed were 1 A cm^{-2} and the calculated j_{cr} curve is well above this current density for typical operating temperatures > 700 °C. Thus, it appears that the present model predicts both the present data and prior results for oxygen electrode delamination.

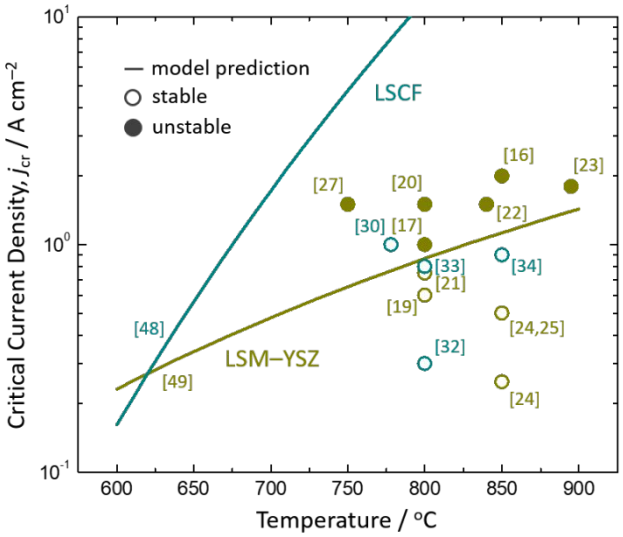

Fig. 14 Experimental observations of fracture (closed symbols) or stable operation (open symbols) for LSM-YSZ and LSCF electrodes operated under different conditions. Shown comparison of the model predicted (eqn 8) critical current densities for fracture versus temperature, using R_p values from the literature.[48,49]

4. Conclusions

The present results show that SOECs tend to fail at higher current density and lower operating temperature, conditions that yield electrode overpotentials that exceed ~0.2 V. The main failure mechanism caused by these conditions is fracture at the electrode/electrolyte interface. Modeling results show that the fracture occurs at this interface because it is the location with a combination of high effective oxygen partial pressure and the low fracture toughness of the perovskite electrode materials compared to those of the electrolyte (YSZ and GDC). Different electrode materials fail under different conditions primarily due to their different electrode polarization resistance values. The model also predicts a peak in the oxygen pressure at the GDC/YSZ interface that probably explains the observation of fracture or oxygen bubble formation near this interface.

5. Experimental

5.1 Cell fabrication

STF and STFC were produced *via* solid state reaction as reported elsewhere.[31,50] The resultant STF/STFC, commercial LSCF (Praxair), and $Ce_{0.9}Gd_{0.1}O_2$ (GDC, Fuelcellmaterials) powders were mixed with vehicle (V-737, Heraeus) in a weight ratio of 1:1.2 in a three-roll mill to prepare the screen-printing paste.

Two types of cells were constructed in this work to examine the electrode/electrolyte degradation: (*i*) An electrolyte-supported symmetric cell and (*ii*) a fuel electrode-supported full

cell. For the symmetric cell fabrication, the YSZ electrolyte support with thicknesses of ~400 μm was prepared by tape casting, lamination, and sintering.[31,51] Note that 1 mol.% Fe_2O_3 (Alfa Aesar, 99.8 %) was added as a sintering aid into the YSZ to achieve a sufficiently high density at a reduced temperature of 1250 °C.[51] The porous oxygen electrode with active area of 0.5 cm^2 and GDC diffusion barrier layer were screen-printed symmetrically on both sides of the YSZ support and then sintered, as described previously.[31,38,46,51] For the fabrication of fuel electrode-supported full cell, the NiO–YSZ supported half-cells were prepared through tape casting and lamination using 45 wt.% NiO–45 wt.% YSZ–10 wt.% starch (as a support), 50 wt.% NiO–50 wt.% YSZ (as a fuel electrode functional layer), and YSZ with 1 mol.% Fe_2O_3 sintering aid (as an electrolyte). The resultant laminates were then co-sintered at 1250 °C. Lastly, the GDC barrier layers and oxygen electrodes (active area: 0.5 cm^2) were formed via screen-printing onto the YSZ electrolyte layer of the half-cell. After firing at 1250 °C for 2 h for GDC and then 1050 °C for 3 h for STF, the STF layers were found to be ~ 8 μm thick and the GDC layers were ~ 2.5 μm thick.

5.2 Electrochemical characterization

For the symmetric cell testing, gold grids (Heraeus) were screen-printed on both electrodes to improve current collection. For the three-electrode measurements, an Ag reference electrode (Heraeus) was brush-painted as a ring at the edge of symmetric cell, as shown in Fig. S7 (in the Supporting Information). The life tests were carried out on the symmetric cells with STF, STFC, and LSCF electrodes, by using various dc electrolysis current densities of 0.4, 0.8, and 1.6 A cm^{-2} (Keysight U8001A) at 600–800 °C in air. The electrochemical impedance spectroscopy was carried out with a Bio-Logic SP-300 and an IM6 Electrochemical Workstation (ZAHNER) by using a 20 mA ac signal in the frequency range of from 0.1 Hz to 100 kHz.

For the full cell testing, the gold grids were applied on the oxygen electrode through screen-printing for current collection. The cells were mounted/sealed on alumina tubes by using silver paste (DAD-87, Shanghai Research Institute of Synthetic Resins). During the electrolysis testing, 50 vol.% H_2O humidified and air were supplied into the fuel and oxygen electrodes, respectively, and the cell voltages were recorded through a LabView controlled Keithley sourcemeter.

5.3 Materials characterization

The microstructural observation and surface chemistry were performed on the post-test cells through scanning electron microscopy (SEM, Hitachi S-4800) combined with energy-dispersive X-ray spectroscopy (EDS, Oxford INCA).

Conflicts of interest

There are no conflicts to declare.

Acknowledgements

The authors gratefully acknowledge research support from the HydroGEN Advanced Water Splitting Materials Consortium, established as part of the Energy Materials Network under the U.S. Department of Energy, Office of Energy Efficiency and Renewable Energy, Fuel Cell Technologies Office, under Award Number DE-0008079.

References

1 H. Wuester, R. Ferroukhi, L. El-Katiri, D. Saygin, T. Rinke and D. Nagpal, *REthinking Energy: Renewable Energy and Climate Change (http://www.irena.org/rethinking/default2015.aspx)*, International Renewable Energy Agency, 2015.
2 P. Denholm, E. Ela, B. Kirby and M. Milligan, *The Role of Energy Storage with Renewable Electricity Generation (http://www.nrel.gov/docs/fy10osti/47187.pdf)*, 2010.
3 S. H. Jensen, C. Graves, M. Mogensen, C. Wendel, R. Braun, G. Hughes, Z. Gao and S. A. Barnett, *Energy Environ. Sci.*, 2015, **8**, 2471 - 2479.
4 M. Mogensen, S. H. Jensen, A. Hauch, I. Chorkendorff and T. Jacobsen, *Ceram Eng Sci Proc*, 2008, **28**, 91-101.
5 B. Dunn, H. Kamath and J. -M. Tarascon, *Science*, 2011, **18**, 928-935.
6 Z. Yang, J. Zhang, M. C. W. Kintner-Meyer, X. Lu, D. Choi, J. P. Lemmon and J. Liu, *Chemical Reviews*, 2011, **111**, 3577-3613.
7 D. M. Bierschenk, J. R. Wilson and S. A. Barnett, *Energy & Environmental Science*, 2011, **4**, 944.
8 S. Gopalan, M. Mosleh, J. J. Hartvigsen and R. D. McConnell, *Journal of Power Sources*, 2008, **185**, 1328-1333.
9 W. Smith, *Journal of Power Sources*, 2000, **86**, 74-83.
10 A. Hauch, S. D. Ebbesen, S. H. Jensen and M. Mogensen, *Journal of Materials Chemistry*, 2008, **18**, 2331.
11 C. H. Wendel, Z. Gao, S. A. Barnett and R. J. Braun, *Journal of Power Sources*, 2015, **283**, 329-342.
12 J. B. Hansen, presented in part at the Manufacturing of Green Fuels from Renewable Energy (https://files.conferencemanager.dk/medialibrary/010c1367-e991-4a33-ab10-1953247e9c23/images/JohnBogildHansen_HaldorTopsoe_Risoe_April_2015.pdf), Roskilde, Denmark, 2015.
13 A. V. Virkar, *International Journal of Hydrogen Energy*, 2010, **35**, 9527-9543.
14 Y. Dong and I.-W. Chen, *Journal of the American Ceramic Society*, 2018, **101**, 1058-1073.
15 A. V. Virkar, in *Engineered Ceramics*, John Wiley & Sons, Inc., 2016, DOI: 10.1002/9781119100430.ch4, pp. 59-76.
16 R. Knibbe, M. L. Traulsen, A. Hauch, S. D. Ebbesen and M. Mogensen, *Journal of The Electrochemical Society*, 2010, **157**, B1209-B1217.
17 X. Sun, M. Chen, Y.-L. Liu, P. Hjalmarsson, S. D. Ebbesen, S. H. Jensen, M. B. Mogensen and P. V. Hendriksen, *Journal of The Electrochemical Society*, 2013, **160**, F1074-F1080.
18 J. R. Mawdsley, J. David Carter, A. Jeremy Kropf, B. Yildiz and V. A. Maroni, *International Journal of Hydrogen Energy*, 2009, **34**, 4198-4207.
19 P. Kim-Lohsoontorn, N. Laosiripojana and J. Bae, *Current Applied Physics*, 2011, **11**, S223-S228.
20 P. Hjalmarsson, X. Sun, Y.-L. Liu and M. Chen, *Journal of Power Sources*, 2013, **223**, 349-357.
21 M. Chen, J. V. T. Høgh, J. U. Nielsen, J. J. Bentzen, S. D. Ebbesen and P. V. Hendriksen, *Fuel Cells*, 2013, **13**, 638-645.
22 M. Keane, M. K. Mahapatra, A. Verma and P. Singh, *International Journal of Hydrogen Energy*, 2012, **37**, 16776-16785.
23 M. A. Laguna-Bercero, R. Campana, A. Larrea, J. A. Kilner and V. M. Orera, *Journal of Power Sources*, 2011, **196**, 8942-8947.

24 C. Graves, S. D. Ebbesen and M. Mogensen, *Solid State Ionics*, 2011, **192**, 398-403.
25 S. D. Ebbesen, J. Høgh, K. A. Nielsen, J. U. Nielsen and M. Mogensen, *International Journal of Hydrogen Energy*, 2011, **36**, 7363-7373.
26 K. Chen and S. P. Jiang, *International Journal of Hydrogen Energy*, 2011, **36**, 10541-10549.
27 J. Kim, H.-I. Ji, H. P. Dasari, D. Shin, H. Song, J.-H. Lee, B.-K. Kim, H.-J. Je, H.-W. Lee and K. J. Yoon, *International Journal of Hydrogen Energy*, 2013, **38**, 1225-1235.
28 G. A. Hughes, J. G. Railsback, K. J. Yakal-Kremski, D. M. Butts and S. A. Barnett, *Faraday Discuss.*, 2015, **182**, 365-377.
29 C. Graves, S. D. Ebbesen, S. H. Jensen, S. B. Simonsen and M. B. Mogensen, *Nature materials*, 2015, **14**, 239-244.
30 F. Tietz, D. Sebold, A. Brisse and J. Schefold, *Journal of Power Sources*, 2013, **223**, 129-135.
31 S.-L. Zhang, H. Wang, M. Y. Lu, A.-P. Zhang, L. V. Mogni, Q. Liu, C.-X. Li, C.-J. Li and S. A. Barnett, *Energy & Environmental Science*, 2018, DOI: 10.1039/c8ee00449h.
32 G. Schiller, A. Ansar, M. Lang and O. Patz, *Journal of Applied Electrochemistry*, 2009, **39**, 293-301.
33 S. J. Kim and G. M. Choi, *Solid State Ionics*, 2014, **262**, 303-306.
34 J. Schefold, A. Brisse and H. Poepke, *International Journal of Hydrogen Energy*, 2017, **42**, 13415-13426.
35 Z. Pan, Q. Liu, L. Zhang, X. Zhang and S. H. Chan, *Journal of The Electrochemical Society*, 2015, **162**, F1316-F1323.
36 Z. Gao, L. V. Mogni, E. C. Miller, J. G. Railsback and S. A. Barnett, *Energy & Environmental Science*, 2016, **9**, 1602-1644.
37 S. P. Simner, M. D. Anderson, M. H. Engelhard and J. W. Stevenson, *Electrochemical and Solid-State Letters*, 2006, **9**, A478-A481.
38 H. Wang, K. J. Yakal-Kremski, T. Yeh, G. M. Rupp, A. Limbeck, J. Fleig and S. A. Barnett, *Journal of The Electrochemical Society*, 2016, **163**, F581-F585.
39 C. Chatzichristodoulou, M. Chen, P. V. Hendriksen, T. Jacobsen and M. B. Mogensen, *Electrochimica Acta*, 2016, **189**, 265-282.
40 T. Jacobsen, C. Chatzichristodoulou and M. Mogensen, *ECS Transactions*, 2014, **61**, 203-214.
41 T. Jacobsen and M. Mogensen, *ECS Transactions*, 2008, **13**, 259-273.
42 M. Mogensen and T. Jacobsen, *ECS Transactions*, 2009, **25**, 1315-1320.
43 M. Chen, Y.-L. Liu, J. J. Bentzen, W. Zhang, X. Sun, A. Hauch, Y. Tao, J. R. Bowen and P. V. Hendriksen, *Journal ofThe Electrochemical Society*, 2013, **160**, F883-F891.
44 A. V. Virkar, in *Engineered Ceramics: Current Status and Future Prospects*, The American Ceramic Society and John Wiley & Sons, Inc., 2016, ch. 4.
45 J. Laurencin, G. Delette, B. Morel, F. Lefebvre-Joud and M. Dupeux, *Journal of Power Sources*, 2009, **192**, 344–352.
46 J. G. Railsback, H. Wang, Q. Liu, M. Y. Lu and S. A. Barnett, *Journal ofThe Electrochemical Society*, 2017, **164**, F3083-F3090.
47 A. P. Sakhya, J. Maibam, S. Saha, S. Chanda, A. Dutta, B. I. Sharma, R. K. Thapa and T. P. Sinha, *Indian Journal of Pure & Applied Physics*, 2015, **53**, 102-109.
48 M. Liu, D. Ding, K. Blinn, X. Li, L. Nie and M. Liu, *International Journal of Hydrogen Energy*, 2012, **37**, 8613-8620.
49 J. R. Wilson, A. T. Duong, M. Gameiro, H.-Y. Chen, K. Thornton, D. R. Mumm and S. A. Barnett, *Electrochemistry Communications*, 2009, **11**, 1052-1056.
50 S. Cho, D. E. Fowler, E. C. Miller, J. S. Cronin, K. R. Poeppelmeier and S. A. Barnett, *Energy & Environmental Science*, 2013, **6**, 1850-1857.
51 Z. Gao, V. Y. Zenou, D. Kennouche, L. Marks and S. A. Barnett, *Journal of Materials Chemistry A*, 2015, **3**, 9955-9964.

Broader context

The International Renewable Energy Agency has determined that half of the CO_2 emissions reductions needed to limiting global warming to 2 ^oC can be achieved by increasing renewables such as wind and solar to 36 % of energy production by 2030. However, these renewables provide an intermittent and in some cases unpredictable supply; when they exceed ~20 % of total electricity generation, energy storage is required to match supply with demand while avoiding curtailment. The SOEC technology addressed in this report is a promising contender for large-scale grid electricity storage and for conversion of excess renewable electricity to useful fuels for transportation and other applications. Given that good long-term stability is a key requirement for viability of this technology, the fundamental understanding of oxygen-electrode degradation phenomena developed in the present study is expected to play an important role in its further development.